JMEPEG (2024) 33:8340–8353
https://doi.org/10.1007/s11665-023-08519-8

1059-9495/$19.00

ORIGINAL RESEARCH ARTICLE

Numerical Model for Simulation of Melting and Microstructure Evolution during a Multi-layered Laser Melting Process

Aurabinda Swain, M. Jegatheesan, Amman Jakhar, Prasenjit Rath, and Anirban Bhattacharya

Submitted: 22 May 2023 / Revised: 29 June 2023 / Accepted: 8 July 2023 / Published online: 20 July 2023

In this paper, a numerical model is presented for the simulation of melting and microstructure formation during a layer-by-layer laser melting process. The model couples the solution of thermal and species transport with a sharp-interface enthalpy-based phase change model to track the melting and solidification in each layer. The effect of the moving laser energy source is implemented through a transient moving heat flux boundary condition. Transition from the completion of a layer to the start of a new layer is implemented using a domain translation technique, keeping the size of the computational domain constant. The model captures the remelting of a previous layer during the formation of a new layer. Simulations are performed to predict the segregation and grain structure formation during multi-layered laser melting of Al-10%Cu alloy. It is seen that the laser scan direction governs the grain orientation with grains growing in the direction of laser travel. Also, the remelting of the previously formed grains in the adjacent layer affects the species concentration and grain structure in the subsequent layer. Higher power, lower laser scan speed, and smaller laser radius leads to the formation of longer grains with larger aspect ratio spanning multiple layers.

Keywords additive manufacturing, grain remelting, layer-by-layer laser melting, microstructure evolution, thermal and species transport

1. Introduction

Additive manufacturing, also known as 3D printing, is a layer-by-layer material deposition process. In metal additive manufacturing (MAM) (Ref 1-5), the raw material can be in different forms, such as powder, wire, sheet and preplaced powder bed. The material is subjected to melting in a defined manner with the help of energy sources such as lasers (Ref 6, 7), electron beams (Ref 8, 9) and electric arcs (Ref 10, 11). After removing the energy source, the molten material loses heat and solidifies to form the desired product. Use of additive manufacturing has considerable potential in automobile, medical, energy and aerospace applications due to its ability to produce complex shapes, efficient use of raw materials, and flexibility of design modifications compared to conventional manufacturing processes.

Additive manufacturing has been used and studied with different types of alloys, such as aluminum alloys (Ref 12, 13), stainless steel (Ref 14, 15), titanium alloys (Ref 16, 17), and

Aurabinda Swain, M. Jegatheesan, Prasenjit Rath, and **Anirban Bhattacharya**, School of Mechanical Sciences, IIT Bhubaneswar, Argul, Jatni District, Khurda, Odisha 752050, India; and **Amman Jakhar**, Department of Mechanical Engineering, Chandigarh University, Ajitgarh 140413, India. Contact e-mail: anirban@iitbbs.ac.in.

List of Symbols

A	Absorptivity
a, b	Constants
C	Volume-averaged concentration
C_p	Specific heat (J/kgK)
C_m	Mean concentration
C_0	Initial concentration
C_{ck}	Coefficient of flow resistance source term
D	Solute diffusivity (m^2/s)
f_l	Liquid fraction
h	Enthalpy (J/kg)
k	Effective thermal conductivity (W/mK)
k_p	Partition coefficient
L	Latent heat of fusion (J/kg)
m	Equilibrium slope of the liquidus line for binary alloy
n	Nucleation density
n_{max}	Maximum number of nuclei
p	Pressure (N/m^2)
P	Laser power (W)
S	Flow resistance source (N/m^3)
S_b	Buoyancy source term in momentum equation (N/m^3)
S_{cr}	Volumetric source term in energy equation (W/m^3)
T	Temperature (K)
T_m	Melting temperature (K)
T_i	Interface temperature (K)
t	Time (s)
$\vec{u}$	Velocity (m/s)
v_l	Laser travel speed (m/s)
r_0	Laser spot radius (m)
V	Concentration potential
g	Acceleration due to gravity (m/s^2)
x, y	Domain axes

Greek symbols	
β_T	Thermal expansion coefficients (K^{-1})
β_S	Solutal expansion coefficients
γ	Surface tension (N/m)
ϵ	Porosity
θ	Interface angle
θ_r	Crystallographic orientation of dendrite
κ	Curvature (m^{-1})
μ	Dynamic viscosity (Pa.s)
ρ	Density (kg/m^3)
ΔT	Undercooling (K)
ΔT_m	Mean undercooling for nucleation (K)
ΔT_σ	Standard deviation of undercooling for nucleation (K)
σ	Surface tension coefficient (N/mK)
σ_t	Surface tension (N/m)

Subscripts	
l	Liquid phase
s	Solid phase
x, y	With respect to x-axis and y-axis, respectively

nickel alloys (Ref 18, 19). Recently, laser-based additive manufacturing (LAM) has received wide attention due to the ability of using high power density and sharp focus (Ref 20). There are mainly two types of LAM processes, namely laser powder bed fusion (PBF-L) (Ref 21, 22) and laser direct energy deposition (DED-L) (Ref 23, 24). The PBF-L process, also known as selective laser melting (SLM) or direct metal laser melting (DMLM), involves selectively applying a laser to a preplaced powder bed. In the DED-L process, also referred to as laser metal deposition (LMD), the powder or wire is fed so that it interacts with the laser and melts. The laser is also a power source in other multi-pass melting processes, such as laser welding (Ref 25, 26) and laser cladding (Ref 27, 28). Studying different aspects of laser melting such as microstructure evolution (Ref 29), presence of defects such as pore formation (Ref 30), balling effect (Ref 31), surface roughness (Ref 32), mechanical properties (Ref 33), and fracture behavior (Ref 34, 35) is necessary to optimize the laser melting process.

In additive manufacturing, if the substrate and the deposited material are same, the grain growth occurs from the previous layer, similar to the phenomena observed in welding two similar materials (Ref 36). However, new nucleation occurs at the melt pool boundary if the substrate is of a different material, similar to the phenomena observed in the laser cladding process (Ref 37). The grain orientation in additive manufacturing depends on the alloy's crystal structure and maximum heat flow direction (Ref 38). In polycrystalline materials, crystal growth is competitive (Ref 39). The temperature gradient, solidification rate, undercooling, remelting and re-solidification all play important roles in the evolution of the final microstructure (Ref 40). The effect of temperature gradient and solidification rate can be explained by the solidification map given by Kou (Ref 36), in which it is observed that a high temperature gradient results in a planar structure. At a low temperature gradient, an equiaxed dendritic structure is observed. It has also been seen that a high cooling rate makes the grain structure more refined and higher undercooling makes the grains grow faster (Ref 41). A fine microstructure was observed by Thijs et al. (Ref 42) in aluminum alloys manufactured through the SLM process. Through grain structure analysis, Garibaldi et al. (Ref 15) observed a high aspect ratio and grain orientation of columnar grains along the build direction in high silicon alloy SLM samples.

It has been shown that remelting has a prominent effect on the final microstructure. Richter et al. (Ref 43) studied the melt pool dynamics and the effect of remelting on surface finish of Co-Cr alloy developed using the SLM process. Vaithilingam et al. (Ref 44) performed chemical analysis of Ti6Al4V alloy fabricated using the SLM process. The decrease in the oxide layer with depth was found to be the lowest in remelted specimen. Brodie et al. (Ref 45) investigated the effect of the remelting process on Ti25Ta samples developed using the SLM process. It was observed that the remelting process resulted in denser and chemically homogeneous samples. Liu et al. (Ref 46) investigated remelting during selective laser melting of AlSi10Mg alloy using various scanning strategies to reduce surface roughness and obtain denser material while improving metallurgical bonding between two consecutive layers. Boschetto et al. (Ref 47) studied the effect of remelting on the surface roughness of AlSi10Mg alloy parts developed using the LAM process. It was observed that the surface quality improved with an increase in laser energy density. Xiong et al. (Ref 48) studied the effect of remelting on tungsten specimens developed using the SLM process. It was observed that the remelting process resulted in a fine microstructure and a reduction of surface roughness. Okugawa et al. (Ref 49) studied the effects of rapid heating and cooling on microstructure evolution during LAM of Al-Si eutectic alloy and proposed that grain refinement occurs due to heterogeneous nucleation during the remelting process.

Numerical analysis of additive manufacturing (AM) is essential in determining the grain structure, orientation, size, and the effect of important process parameters on these properties. Initial models have focussed on melt pool and heat transfer analysis due to laser-powder interaction (Ref 50-52). Shiomi et al. (Ref 50) performed numerical and experimental studies on the laser prototyping of metallic powders. It was observed that the solidification was affected more by laser power rather than the duration of laser irradiation. Tolochko et al. (Ref 51) simulated the temperature distribution for different laser powers and powder sizes. Dai and Shaw (Ref 52) compared the numerical results obtained using powder and solid bed models. For the powder bed model, high temperature gradients in the bed and asymmetric melt pool were observed. In the solid bed model, low temperature gradients in the bed and a symmetric melt pool were observed. This difference was attributed to the low thermal conductivity of the bed in the powder bed model.

Yin and Felicelli (Ref 53) developed a coupled FEM-cellular automata (CA) model to study dendrite growth during a laser-engineered net shaping (LENS) process. A finer microstructure was observed with increase in laser travel speed, decrease in layer thickness and decrease in substrate thickness. Liu and Qi (Ref 54) developed a model based on the finite difference method (FDM) to analyze the laser deposition of alloy powders. It was observed that the maximum temperature in the melt pool and melt pool size increases in successively deposited layers due to poor heat dissipation through the deposited part. Rai et al. (Ref 55, 56) developed a coupled CA-

lattice Boltzmann (LB) model to study grain growth during the electron beam melting process. It was observed that the scan direction affects the grain orientation during solidification. By changing the scan direction for every successive layer, grain growth along the build direction was obtained. A CA model was developed by Zinoviev et al. (Ref 57) to study the evolution of grain structure during the SLM process. It was reported that the thermal gradient dictates the orientation of grain growth. Zhang et al. (Ref 58) developed a coupled FE-CA model to study grain morphology during the DED process. It was observed that the grain size is larger in the top portion of a layer. It was also observed that the microstructure is dominated by equiaxed grains in the first layer and is dominated by columnar grains with successive deposition of layers.

A Monte Carlo model was developed to study grain growth during the AM process by Rodgers et al. (Ref 59). It was observed that the scan direction, laser powder feed and laser power affect the angle of grain growth. Pauza et al. (Ref 60) studied the crystallographic structure and grain morphology in the LPBF process using the Monte Carlo Potts model. It was observed that the local temperature gradient affects the crystallographic orientation. Sahoo and Chou (Ref 61) developed a phase field model to study microstructure evolution during the electron beam additive manufacturing process. It was observed that the columnar dendritic arm spacing and dendrite width decreased with an increase in scan speed and temperature gradient.

From the study, it is observed that considerable work has been done on microstructure analysis of laser-based additive manufacturing processes. These studies focussed on the growth rate, size, and morphology of grains. However, not many studies are present which includes the transport of species during microstructure evolution in such processes. The primary objective of the present work is to develop a 2D sharp interface model to capture the melting and solidification taking place during a layer-by-layer melting and solidification in a laser-based additive manufacturing process. The model incorporates multiple phenomena such as thermal and species transport, grain nucleation and growth, simultaneous melting and solidification driven by a moving laser source, and formation of multiple layers. Using the model, the effect of process parameters such as laser scan direction and laser power on the final microstructure for the entire multilayered sample are predicted. The model captures the partial remelting of a previously solidified layer, and the subsequent growth of the partially remelted grains. The species redistribution during this remelting process is also predicted.

2. Mathematical and Numerical Model

2.1 Problem Description and Assumptions

For the study, the melting and solidification of Al-10% Cu alloy in a 2D rectangular domain is considered. It is assumed that there is a moving laser heat source at the top surface driving the melting process. The schematic diagram for the process is shown in Fig. 1. The model is developed based on a general framework so that the laser melting of other hypo-eutectic binary alloys can also be simulated. At the top boundary, a Gaussian profile-based heat flux condition is given. To represent the movement of the laser, the location of the heat flux is translated with the specified laser scan speed. The other parts of top surface as well as the other boundaries are given convective and radiative heat loss boundary condition.

For simplification of the problem, the following assumptions are taken into consideration:

1. Equilibrium phase diagram is used for phase change calculations.
2. Convection due to thermal and solutal buoyancy is modeled using the Boussinesq approximation.
3. The effect of temperature dependent surface tension is considered by modifying the velocity boundary condition for the top surface.
4. Shrinkage effect is neglected.
5. Vaporization of the melt pool is not considered.

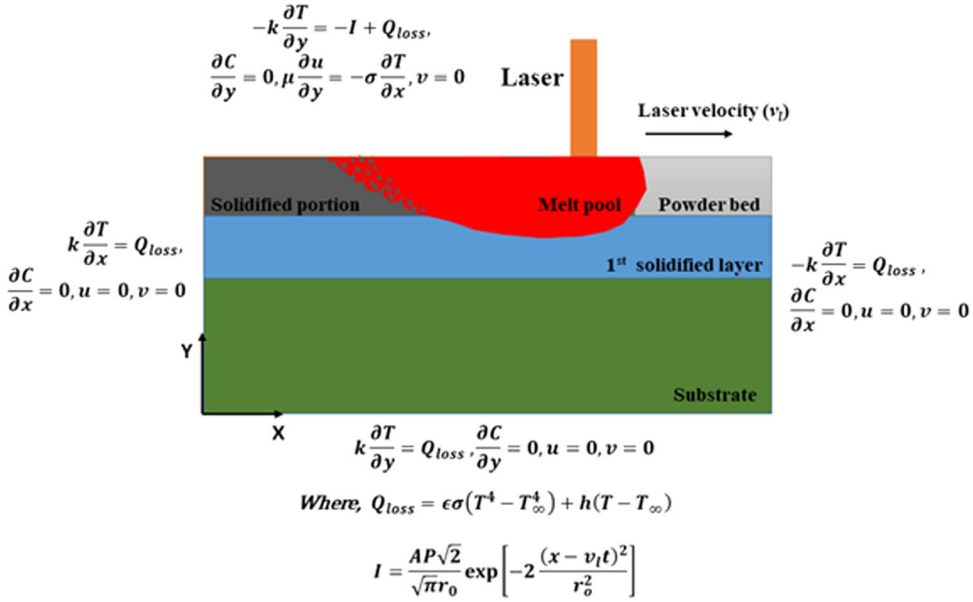

Fig. 1 Schematic diagram of the multilayered laser melting process

The model combines a sharp interface melting and solidification model, energy and species transfer, buoyancy and surface tension driven flow, and a stochastic grain nucleation mechanism. The next subsections describe each of these models in detail.

2.2 Melting and Solidification Model

The melting due to the laser heat flux and the subsequent solidification is governed by the energy transfer in the domain. The evolution of solid–liquid interface during melting and solidification is tracked by defining a liquid fraction variable, f_l, which is calculated from the enthalpy, h, at each discretized control volume. The enthalpy, defined in terms of the temperature T and liquid fraction f_l, as $h = C_pT + f_l$, L is updated by solving the enthalpy-based transient energy conservation equation (Eq 1).

$$\frac{\partial(\rho h)}{\partial t} + \nabla \cdot (\rho \vec{u} h) = \nabla \cdot (k \nabla T) - S_{cr} \quad \text{(Eq 1)}$$

In Eq 1, S_{cr} is a volumetric source term which represents the effect of an imposed cooling rate on the domain. To update the values of f_l, the interface temperature, T_i, needs to be calculated. The interface temperature can be expressed as:

$$T_i = T_m - \frac{T_m \gamma(\theta, \theta_r)\kappa}{L} - m(C_0 - V) \quad \text{(Eq 2)}$$

In Eq 2, T_m is the melting temperature of the alloy corresponding to the initial composition. The 2nd term on right hand side denotes the curvature undercooling which represents the effect of interfacial energy. $\gamma(\theta,\theta_r)$ is the anisotropic surface tension where θ is the angle between interface and domain x-axis and θ_r denotes the orientation of each grain. κ is the curvature of the interface which can calculated from the liquid fraction field as shown in Eq 3 (Ref 62).

$$\kappa = \frac{f_{ly}^2 f_{lxx} - 2 f_{lx} f_{ly} f_{lxy} + f_{lx}^2 f_{lyy}}{\left(f_{lx}^2 + f_{ly}^2\right)^{3/2}} \quad \text{(Eq 3)}$$

The 3rd term on right hand side denotes the solutal undercooling, which is due to the difference of species concentration at the interface from the initial concentration C_0. The species concentration is represented by a concentration potential, V, which is defined as $V = C/(f_l + (1 - f_l)k_p$. C represents the volume-averaged concentration which can be expressed $C = f_l C_l + (1 - f_l)C_s$, where C_l and C_s are the solute concentration in the liquid and solid phases. m and k_p denote the equilibrium slope of the liquidus line and the partition coefficient for the specified alloy.

The concentration field needs to be updated to calculate the interface temperature. To update the concentration field, the volume averaged species conservation equation (Eq 4) is solved.

$$\frac{\partial(\rho C)}{\partial t} + \nabla \cdot (\rho \vec{u} V) = \nabla \cdot (\rho D \nabla V) \quad \text{(Eq 4)}$$

In Eq 4, D is the solute diffusivity defined as $D = f_l D_l + k_p(1 - f_l)D_s$ where D_l and D_s are the solute diffusivities in the liquid and solid phases. The energy and species conservation equations are formulated in terms of volume averaged properties as proposed by Voller (Ref 63). The solidification and dendrite growth model has been presented in detail previously in Jegatheesan and Bhattacharya (Ref 64).

The laser-driven melting is modeled using a moving heat flux boundary condition at the top boundary. It is assumed that the heat flux term follows a Gaussian distribution about the center of the laser beam. This is expressed as

$$I = \frac{AP\sqrt{2}}{\sqrt{\pi} r_0} \exp\left[-2\frac{(x - v_l t)^2}{r_o^2}\right] \quad \text{(Eq 5)}$$

In Eq 5, A is the absorptivity of the alloy surface, P is the laser power, r_0 denotes the laser beam radius, and v_l is the laser scan speed. The sign of v_l is varied depending on the scan direction.

2.3 Flow Model

To incorporate the effect of convection on the phase change process, the mass and momentum conservation equations (Eq 6 and 7) are solved.

$$\nabla \cdot (\rho \vec{u}) = 0 \quad \text{(Eq 6)}$$

$$\frac{\partial(\rho u)}{\partial t} + \nabla \cdot (\rho \vec{u} \vec{u}) = \nabla \cdot (\mu \nabla \vec{u}) - \frac{\partial p}{\partial x} + S_b + S \quad \text{(Eq 7)}$$

In Eq 7, the source term S_b represents the effect of thermal and solutal buoyancy. This is defined using the Boussinesq approximation and can be expressed as $S_b = \rho_l g[\beta_T(T - T_m) + \beta_S(V - C_0)]$. β_T and β_s are the thermal and solutal expansion coefficients. The source term S is included to suppress the flow velocity in the solid phase. It is defined as a function f_l such that the value of S becomes large when $f_l = 0$ and it becomes 0 when $f_l = 1$ (Ref 65). For the present study $S = -C_{ck}\frac{(1-f_l)^2}{b+f_l^3}\vec{u}$ is used, where C_{ck} is given an arbitrary large value. b is introduced to avoid division by 0 when $f_l = 0$.

For including Marangoni convection in the model $\mu\frac{\partial u}{\partial y} = -\sigma\frac{\partial T}{\partial x}$ has been used as velocity boundary condition at top surface. σ is the surface tension cofficient which decreases linearly with increase in temperature as $\sigma = (d\sigma_t/dT)$, where $\sigma_t = a - bT$. Here σ_t is the surface tension. a and b are alloy specific constants. The negative sign is used because in the specified alloy (Al-Cu alloy) the surface tension decreases with increase in temperature.

2.4 Nucleation and Grain Numbering Model

In the present model, the nucleation of new grains needs to be explicitly imposed in the melt pool. To do this, it is assumed that the rate of nucleation is a function of undercooling, similar to the nucleation model given in Rappaz and Gandin (Ref 39). A Gaussian distribution function is used to define the relationship between undercooling and nucleation rate as shown in Eq 8.

$$\frac{dn}{d(\Delta T)} = \frac{n_{max}}{\sqrt{2\pi}\Delta T_\sigma} \exp\left[-\frac{1}{2}\left(\frac{\Delta T - \Delta T_m}{\Delta T_\sigma}\right)^2\right] \quad \text{(Eq 8)}$$

n denotes the nucleation density, ΔT denotes undercooling, ΔT_m and ΔT_σ are the mean and standard deviation of undercooling, and n_{max} is the maximum number of nuclei. Using Eq 8, the number of nuclei corresponding to different

levels of undercooling are calculated and these are distributed randomly in the domain. Each grid with a nucleus is also assigned a critical undercooling value. During the simulation, if the grid is within the melt pool ($f_l = 1$) and has undercooling greater than the corresponding critical undercooling, the nucleation is initiated by making $f_l = 0$ and assigning a grain number to the solid. When the solidification interface of a grain moves to an adjacent cell, the adjacent cell is also assigned the same grain number. Each grain has a unique grain number assigned depending on the sequence of nucleation. The plot of grain number contours is used to show the grain structure during the simulation.

Table 1 Simulation and process parameters

Parameters	Symbol	Values
Domain size, mm × mm	$L \times M$	8 × 4
Number of control volumes	$l_1 \times m_1$	800 × 400
Grid spacing along x and y-axis, mm	Δx *and* Δy	0.01
Time step, ms	Δt	0.0003
Laser power, W	P	500, 100, 1500, 2000
Laser scan speed, m/s	v_l	0.6, 0.8, 1.0, 1.2, 1.4
Laser spot radius, mm	r_0	0.05, 0.08, 0.1, 0.12, 0.15
Initial temperature, K	T_0	300
Initial concentration, %	C_0	10
Absorptivity of laser	A	0.7
Layer thickness, mm	l_t	0.25
Nucleation density, mm^{-2}	n	1000

2.5 Treatment of Multiple Layer Formation

To simulate the melting and solidification of multiple layers, a domain translation technique is used. When one pass of the laser is complete, it is assumed that a new layer with a specified thickness is placed on top of the existing material. To accommodate this new layer, the solution domain is shifted upward by a distance equal to the layer thickness. To maintain consistency with the previous calculations, all the variable values are shifted downward by distance equal to the layer thickness. Thus, the new layer can be included while maintaining the same computational domain size. As a result of this translation, some part of substrate will move out from the lower side of the solution domain and a new powder bed will be added at the top surface. The mechanism of layer shifting with fixed domain size has been explained in detail in Swain et al. (Ref 66).

2.6 Numerical Implementation

The governing equations are discretized using the finite volume method. The domain is divided into 400 × 800

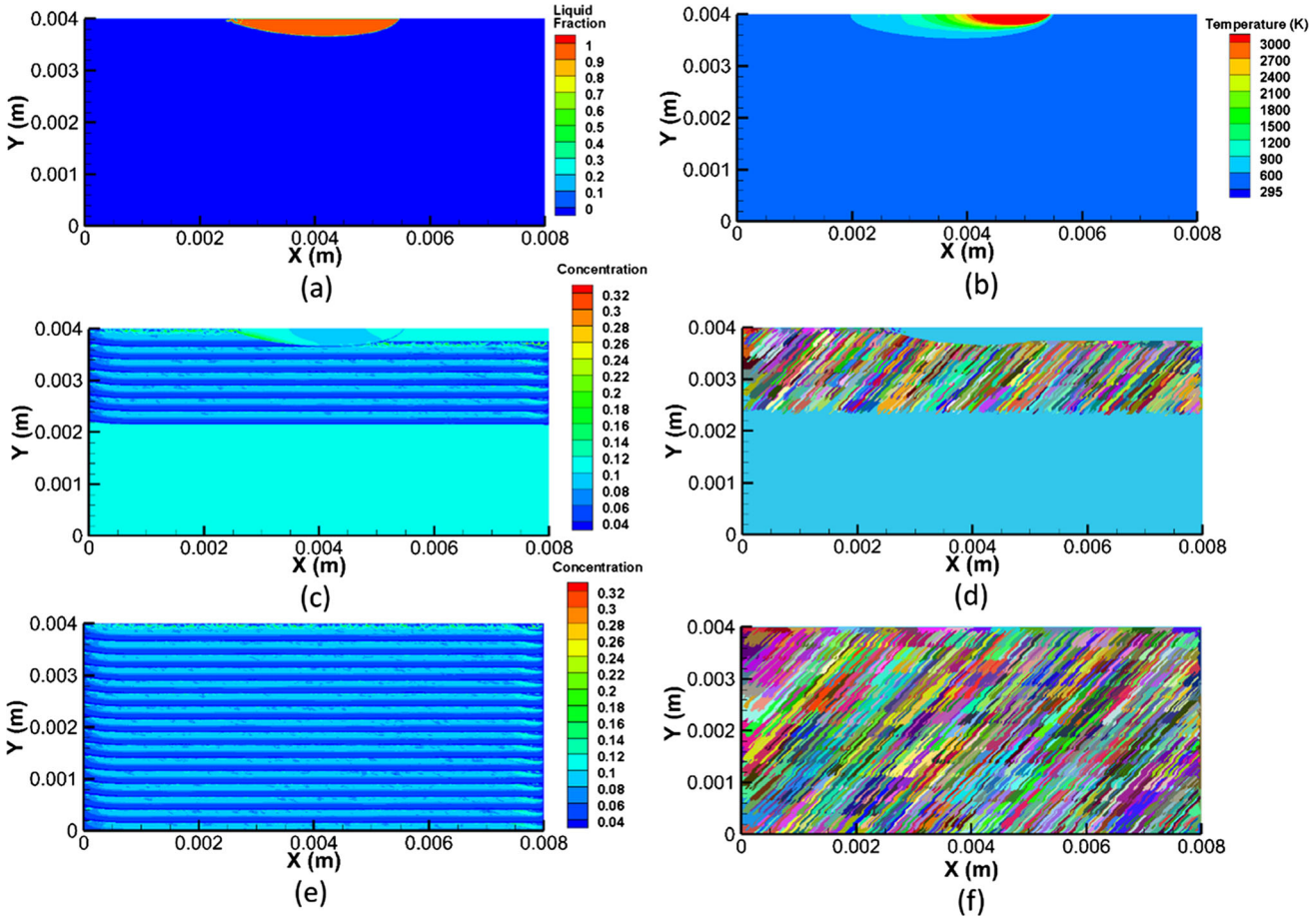

Fig. 2 Unidirectional laser movement from left to right with $P = 1000$ W, $v_l = 1$ m/s: (a) liquid fraction, (b) temperature contour, (c) concentration contour and (d) grain structure for intermediate stage; (e) concentration contour, and (f) microstructure after complete layering of the domain

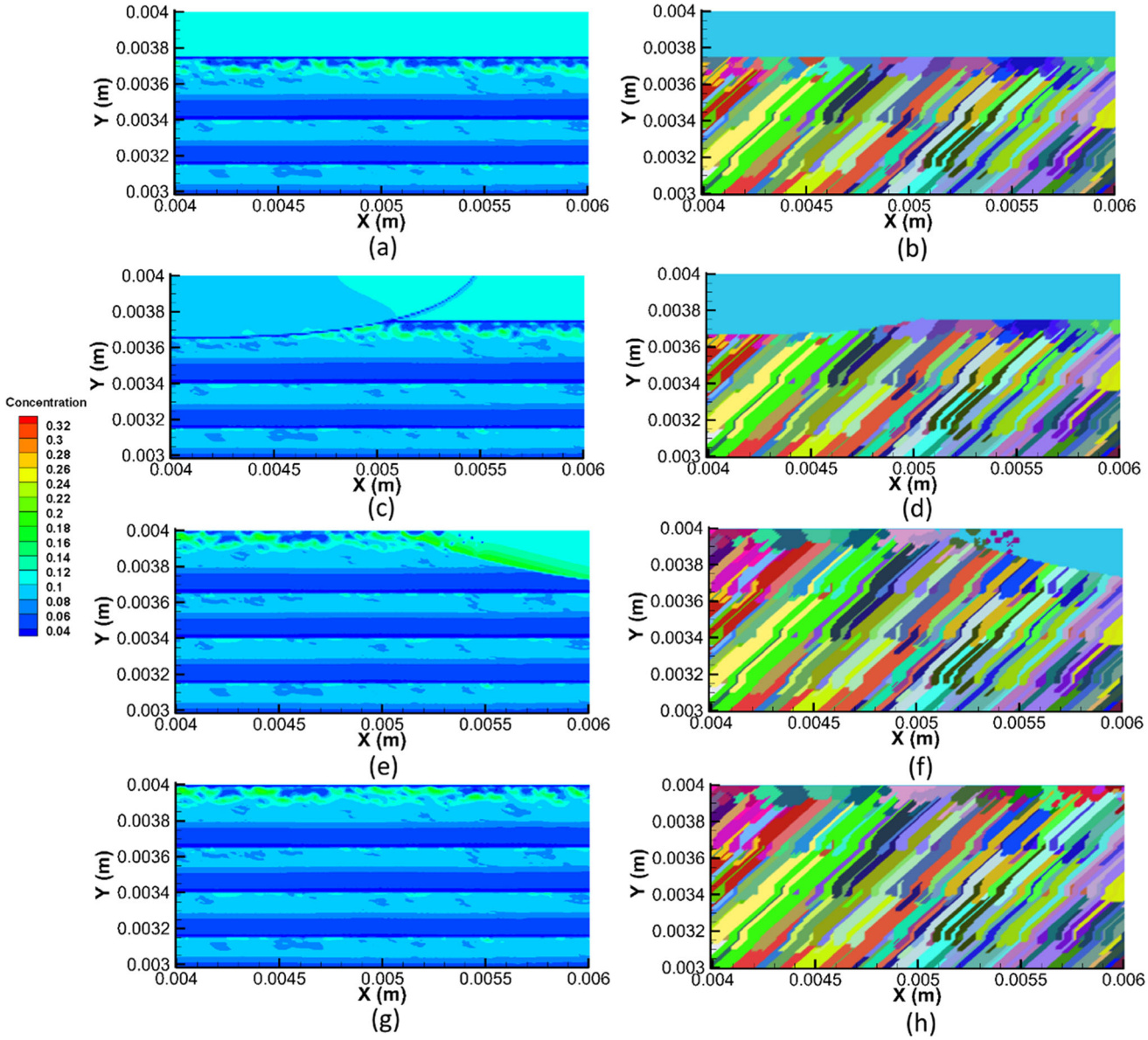

Fig. 3 Enlarged view of the melting and grain growth process for $P = 1000$ W, $v_l = 1$ m/s, where (a), (c), (e) and (g) present the solute concentration contours and (b), (d), (f) and (h) present the microstructure at different time intervals

uniform square grids which equates to a grid spacing of 0.01 mm. The discretized equations are solved by using the line-by-line tri-diagonal matrix algorithm (TDMA) with alternate sweep direction.

In each time step, the energy and species concentration equations (Eq 1 and 4) are solved using the previous time step values of $\vec{u}$, T, f_l and V. From the updated h and C fields, the values of f_l, T and V are obtained. To do this, the temperature-concentration coupling as per the phase diagram is used. The interface temperature, T_i, calculated using Eq 2, is imposed at the interface cells ($0 < f_l < 1$), and the new values of f_l are calculated. Subsequently, the source terms of the momentum equation (Eq 7) are calculated using the updated values of f_l, T and V. The SIMPLER algorithm (Ref 67) is used for solving the momentum and continuity equations. The model is implemented using Fortran 90.

3. Results and Discussion

The developed model is used to simulate the heat transfer, melt pool evolution, species transport, and microstructure formation for a layer-by-layer laser melting process. The base program used for implementing the present model has been validated and utilized previously to predict dendrite growth and microstructure evolution in a domain subjected to given undercooling or cooling rate. Verification of the model and its implementation have been discussed in detail in our previous work (Ref 64, 65). Also, the melting model uses the same mathematical framework presented in Swain et al. (Ref 66). However, unlike the previous work (Ref 66), the present model incorporates features of microscale solidification, such as curvature and solutal undercooling, resolution of solid–liquid interface and nucleation. Thus, the present model can predict

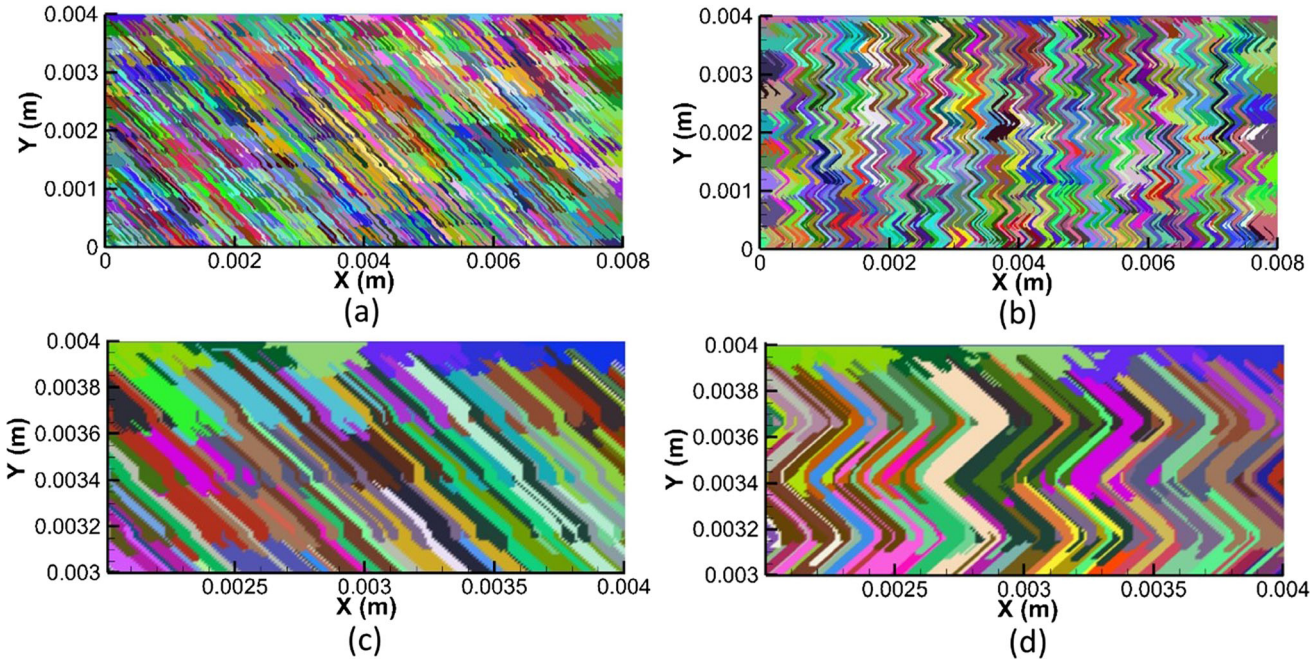

Fig. 4 Unidirectional laser movement from right to left (a) microstructure and (c) zoomed view, and bidirectional laser movement (b) microstructure and (d) zoomed view for P = 1000 W and v_l = 1 m/s

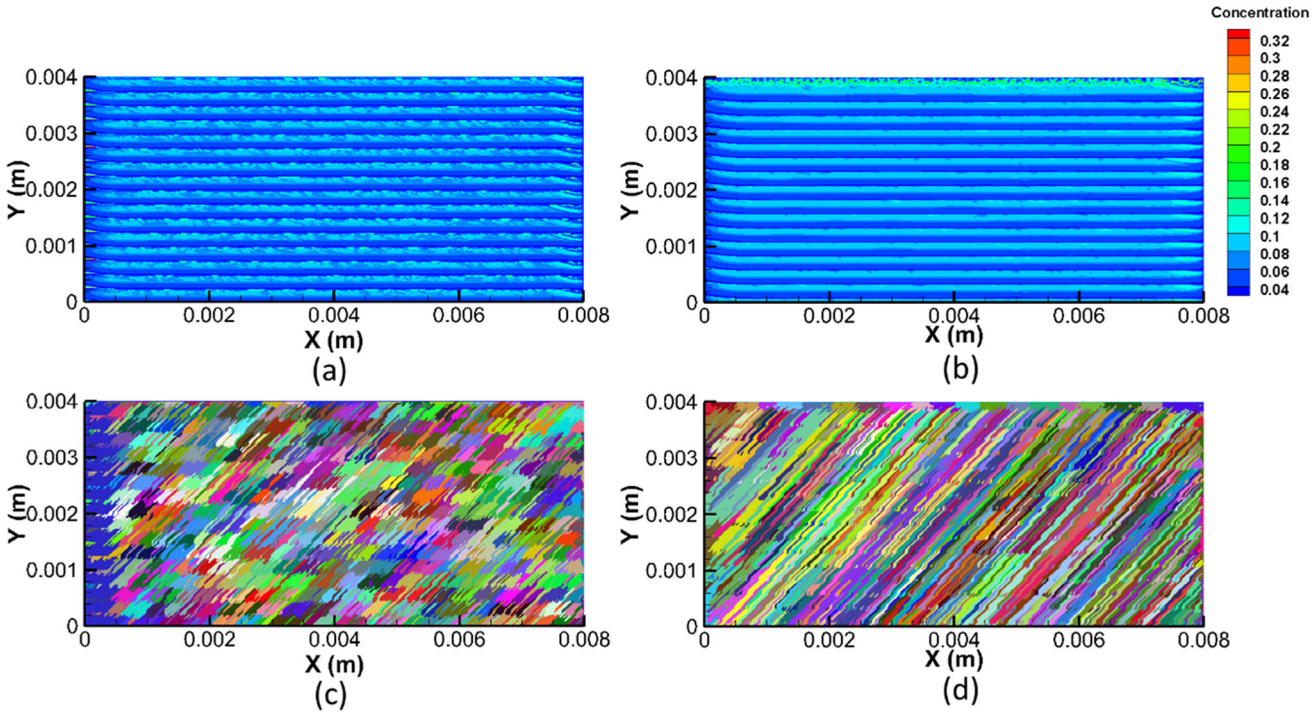

Fig. 5 Effect of laser power: (a) solute concentration contours and (c) microstructure for P = 500 W and v_l = 1 m/s; (b) solute concentration contours and (d) microstructure for P = 2000 W and v_l = 1 m/s

the formation of microstructure from a laser driven melt pool, remelting of the previous microstructure during the melting of new layer, and reformation of grain structure and redistribution of species.

In this section, at first the effect of a moving laser on the formation of a multilayer sample is studied. Next, the effect of unidirectional and bidirectional laser scanning is compared. This is followed by parametric study on the effect of important process parameters such as laser power, laser scan speed, and laser spot radius. The simulation predictions are also qualitatively compared with the results represented in previous studies.

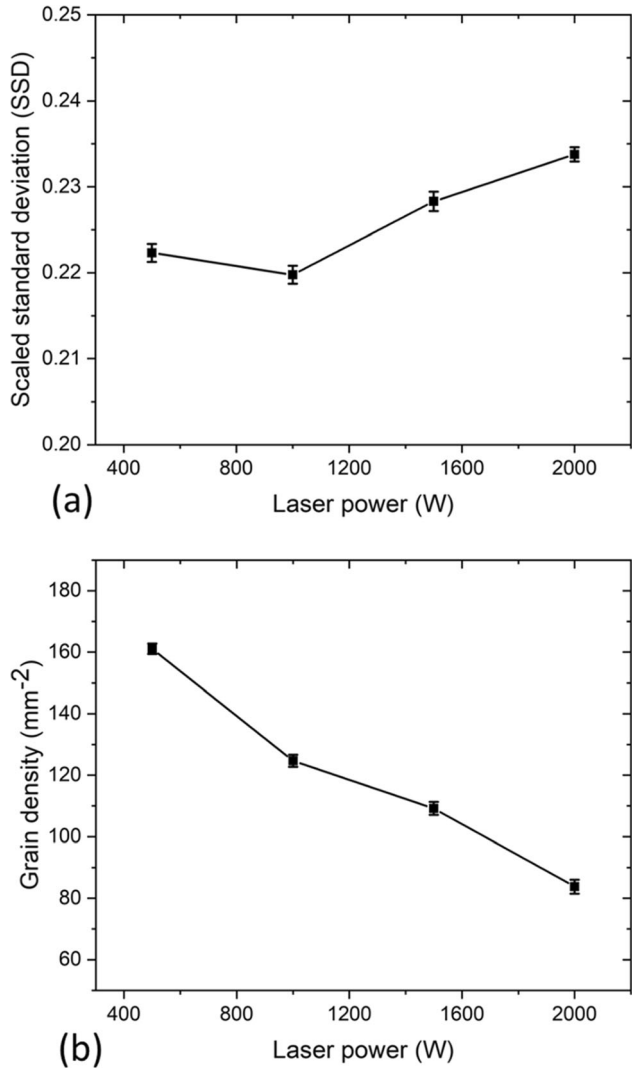

Fig. 6 Effect of laser power on (a) SSD of species concentration and (b) grain density

3.1 Multilayered Laser Melting and Microstructure Evolution

To observe the microscale melting and solidification pattern, the laser melting of multiple layers of Al-10% Cu is simulated. For this, a 2D rectangular domain of size 8 mm by 4 mm is considered. It is assumed that the laser movement is from the left to the right for all the layers. The laser power (P), scan speed (v_l), and spot radius (r_0) are taken as 1000 W, 1 m/s, and 0.1 mm, respectively. The layer thickness is taken as 0.25 mm. The formation of 20 layers is considered. The layer transition is implemented in the model by the use of the domain translation technique discussed previously in section 2.5. The values of all the simulation and process parameters are given in Table 1.

The melt pool shape, temperature and concentration contours, and grain structure during the simulated laser melting process are shown in Fig. 2. From the liquid fraction contours (Fig. 2a), it is seen that the melt pool is asymmetric in shape with a shorter front section and longer trailing edge. This is due to the laser movement which causes the thermal profile to be asymmetric about the laser beam axis. From Fig. 2(b), it can be seen that the thermal gradient is very high near the forward edge of the pool and significantly lower near the trailing edge. As the laser moves from left to right, the region toward the left side of the melt pool has already been under the influence of the laser heat source. In contrast, the region at the right side of the melt pool has not yet been traversed by the laser. Thus, the temperature decreases sharply from the high temperature of the melt pool to the low-temperature unmelted region resulting in a higher temperature gradient. The melting proceeds adjacent to the front edge of the melt pool while solidification occurs near the trailing edge. On careful observation, the formation of new grains near the trailing edge is also seen.

Figure 2(c) and (d) shows the concentration contours and grain structure at an intermediate stage of the simulation. The presence of multiple layers is clearly seen from the concentration variation. The concentration at the bottom of each layer is significantly lower as compared to the top region. All the layers show a similar pattern with horizontal segregation. Figure 2(d) shows the grain structure at the same time as Fig. 2(a), (b), and (c). The plot for the grain structure is generated by using the grain number field. It is seen that grains are inclined in the direction of the laser movement. In general, the grains have high aspect ratio with considerably larger length as compared to their width. Also, the grain formation in each new layer happens by the growth of grains formed previously in the lower layer.

Figure 2(e) and (f) shows the final concentration variation and microstructure in the entire domain. It is seen that the concentration variation is mainly governed by the layering process and depends on the layer thickness. The final microstructure shows long inclined grains spanning multiple layers. Formation of similar microstructure, with grain inclined toward the laser scan direction, has also been shown in previous experimental (Ref 68) and numerical studies (Ref 55, 56, 69-72). The number of grains depends on the specified nucleation parameters and can change for other values of nucleation parameters. However, for all the simulations performed in this study, the nucleation parameter values are kept constant so that the effect of process parameters can be predicted.

During the formation of a new layer there is remelting of the upper portion of the previous layer. To observe this clearly and see its effect on the species redistribution and grain remelting, an enlarged view (2 × 1 mm) of a section of the domain around a trailing edge is plotted in Fig. 3. Figure 3(a), (c), (e), and (g) shows the concentration contours before, during, and after the formation of the melt pool, while Fig. 3(b), (d), (f), and (h) shows the corresponding grain structures. The lower part of each figure shows the previously solidified layers. The upper part represents a new layer bed before its melting. It can be seen that in a new layer the species concentration is uniform before melting (Fig. 3a). There is a clear demarcation in the melt pool with the remelting of the previous layer influencing the current melt pool (Fig. 3c). The upper part of the front section of the melt pool is not affected by the redistribution of species during remelting. The travel of the melt pool causes the solute accumulation near the trailing edge (Fig. 3e). This is limited to

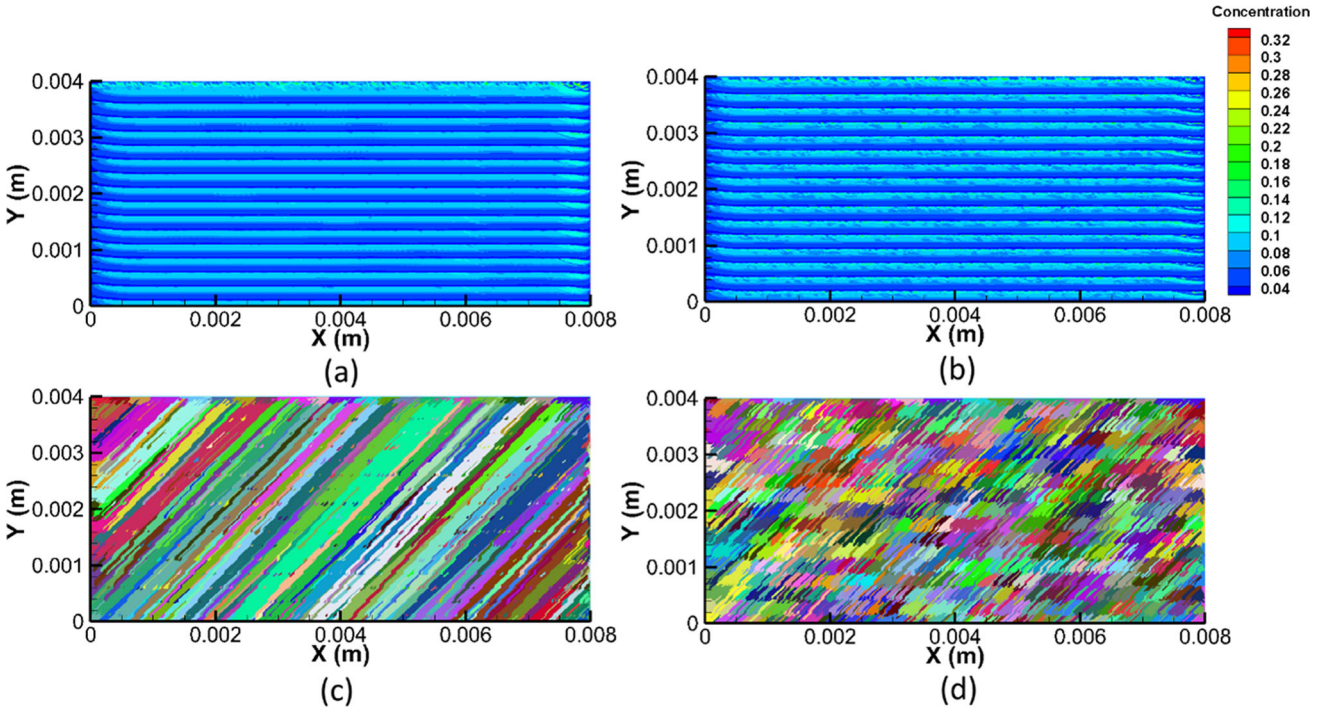

Fig. 7 Effect of laser scan speed: (a) solute concentration contours and (c) microstructure for $P = 500$ W and $v_l = 0.6$ m/s; (b) solute concentration contours and (d) microstructure for $P = 2000$ W and $v_l = 1.4$ m/s

a narrow region due to the high laser scanning speed and solidification rate. After solidification (Fig. 3g), the concentration variation in the layer shows three distinct regions separated horizontally. The concentration at the bottom of the layer is lower as compared to the intermediate region. The top portion shows non-uniform solid distribution due to nucleation and formation of new grains. The lower layers do not show this region as they get remelted during the formation of the immediate upper layer.

Comparing the grain structures before and during melting shows that the previous grains get remelted (Fig. 3b and d). This results in the growth of the previous grains during the solidification of the new layer. As a result, there are elongated grains spanning multiple layers (Fig. 3f). It is also seen that there is nucleation of new grains near the trailing edge of the melt pool. This results in the formation of smaller equiaxed grains at the top of the layer. However, these grains get remelted during the formation of a new layer and thus cannot be seen in the final microstructure.

3.2 Effect of Laser Scan Direction

It has been shown in the literature that the laser scan direction plays an important role in determining the grain morphology during the laser melting process (Ref 57, 59, 70). In particular, Rodgers et al. (Ref 59) has shown that the laser movement from the left to right leads to grain inclination toward the right side while the opposite occurs when the laser scan direction is reversed. To find whether the present model can capture this phenomena two additional simulations are performed—unidirectional laser movement from right to left for each layer, and bidirectional laser movement with reversal of direction for each alternate layer. All the other parameter values are kept same as given in section 3.1.

The simulated microstructure for these two cases are presented in Fig. 4(a) and (b). It can be seen that the grain morphology and orientation are strongly affected by the scan direction. For unidirectional laser movement (Fig. 2f and 4a), all the grains are orientated in the direction of laser travel. Comparing Fig. 2(f) and 4(a), it is observed that the grains grow from left to right when the laser movement occurs from the left side of the domain. The opposite behavior, with grains growing from right to left is seen when laser direction is reversed for all the layers. The grains also have elongated shape with high aspect ratio covering multiple layers.

On the other hand, when the laser travel direction is reversed for alternate layers, the direction of grain growth also changes from one layer to the next layer. This leads to a final grain morphology which is different from those for the unidirectional cases. These changes can be seen more clearly from the enlarged views presented in Fig. 4(c) and (d). The movement of the melt pool dictates the thermal gradient near the solidification interface and thus leads to the directionality of the final grain structure.

3.3 Effect of Process Parameters

In this section, the effect of laser power, laser scan speed and laser spot size on the species segregation and grain morphology are studied. These laser parameters are similar to those in

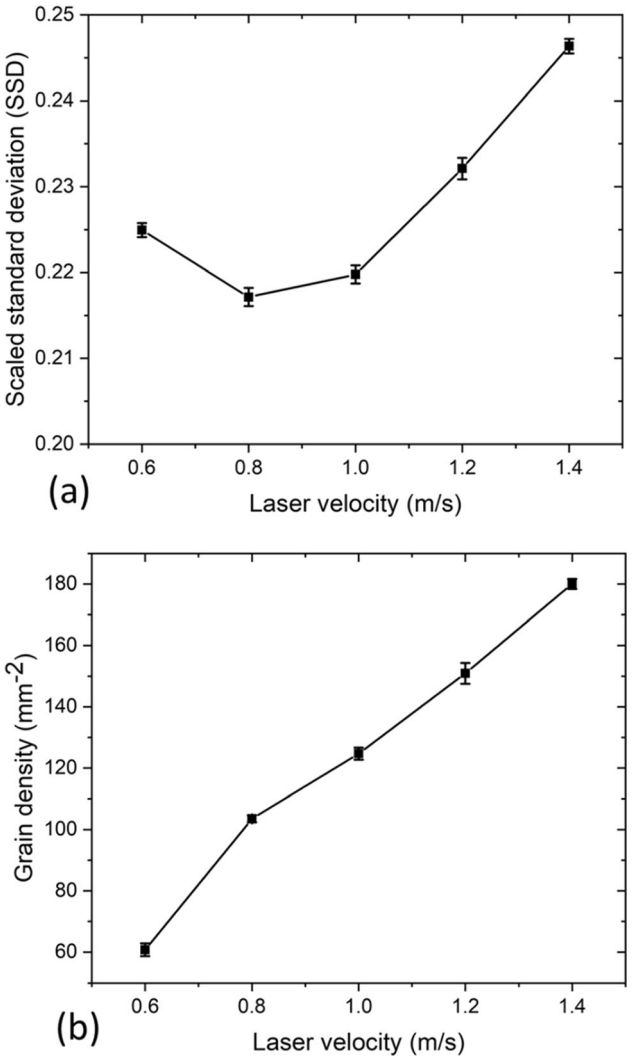

Fig. 8 Effect of laser scan speed on (a) SSD of species concentration and (b) grain density

previous experimental studies carried out by Jelis et al. (Ref 73), Criales et al. (Ref 74) and Nayak et al. (Ref 75). At first, simulations are performed with different laser power values (500, 1000, 1500, 2000 W) keeping all other parameter values same as that given in section 3.1. The values are taken similar to the values used for different laser powder bed fusion processes (Ref 76-78). Figure 5(a) and (b) shows the concentration contours for $P = 500$ and 2000 W. The corresponding simulated microstructures are presented in Fig. 5(c) and (d).

It is seen that the laser power affects the species segregation and grain morphology. For the lower power ($P = 500$ W), there is less segregation and each layer shows two distinct regions—lower part with less concentration and upper part with slightly higher concentrations. In contrast, for the high power case ($P = 2000$ W), there is more segregation and a newly formed layer has three regions with different concentrations. However, due to the larger melt pool depth, the top portion of the previous layer gets remelted during the formation of the subsequent layer and is not present in the final solidified specimen.

The grain structure becomes more elongated with higher power. Longer grains with high aspect ratio are present for the high power case. For the higher laser power case, the melt pool depth is larger which leads to the partial remelting of the grains in the previous layer. During solidification, these grains continue growing in the new layer, resulting in the elongated morphology. For the lower power case, shorter grains with higher width are observed.

To quantify the effect of laser power, a parameter termed as scaled standard deviation (SSD) of species concentration is defined, as given in Eq 9.

$$(\mathrm{SSD}) = \frac{\text{Standard deviation of concentration}}{\text{Mean concentration}} = \frac{\sqrt{\sum_{i,j}(C(i,j) - C_{\mathrm{m}})^2}}{C_{\mathrm{m}}} \quad \text{(Eq 9)}$$

In Eq 9, $C(i,j)$ denotes the solute concentration for the i, j control volume where i represents the index of the control volume in the x direction and j represents the index in the y direction. The mean concentration value is given by C_m. The SSD is a measure of the non-uniformity of species distribution in the solidified layers. The variation of SSD with laser power is plotted in Fig. 6(a). For each value of power, 6 simulations are run and the average values for the studied parameters are plotted. It is seen that there is a small variation, with higher values for higher laser power. This agrees with the observation from Fig. 5(a) and (b).

To quantify the effect of laser power on the microstructure, the grain density in the solidified structure for different values of laser power are plotted in Fig. 6(b). It is seen that the grain density decreases with increasing power. This is due to the formation of long elongated grains at higher power as discussed in relation to Fig. 5(c) and (d).

Next, the effect of laser scan speed is studied. 5 different values are considered: 0.6, 0.8, 1.0, 1.2 m/s. All the other parameters are assigned the same value as those given in section 3.1. Figure 7(a) and (b) shows the concentration contours for 0.6 and 1.4 m/s scan speed. Figure 7(c) and (d) presents the corresponding grain structures after completion of all the layers. Qualitatively, not much difference is observed between the segregation pattern. However, the grain structure plots show considerable difference with longer grains spanning multiple layers at the lower scan speed of 0.6 m/s and shorter grains for the higher scan speed. Lower velocity results in larger remelting of the previous layer grains. The same grains continue growing during the solidification of the subsequent layer. On the other hand, at higher scan speed, the remelting is less and new grains get nucleated resulting in smaller grains.

The segregation and grain densities for different scan speeds are quantitatively compared in Fig. 8. It is seen that the SSD decreases with the increase in scan speed and then increases

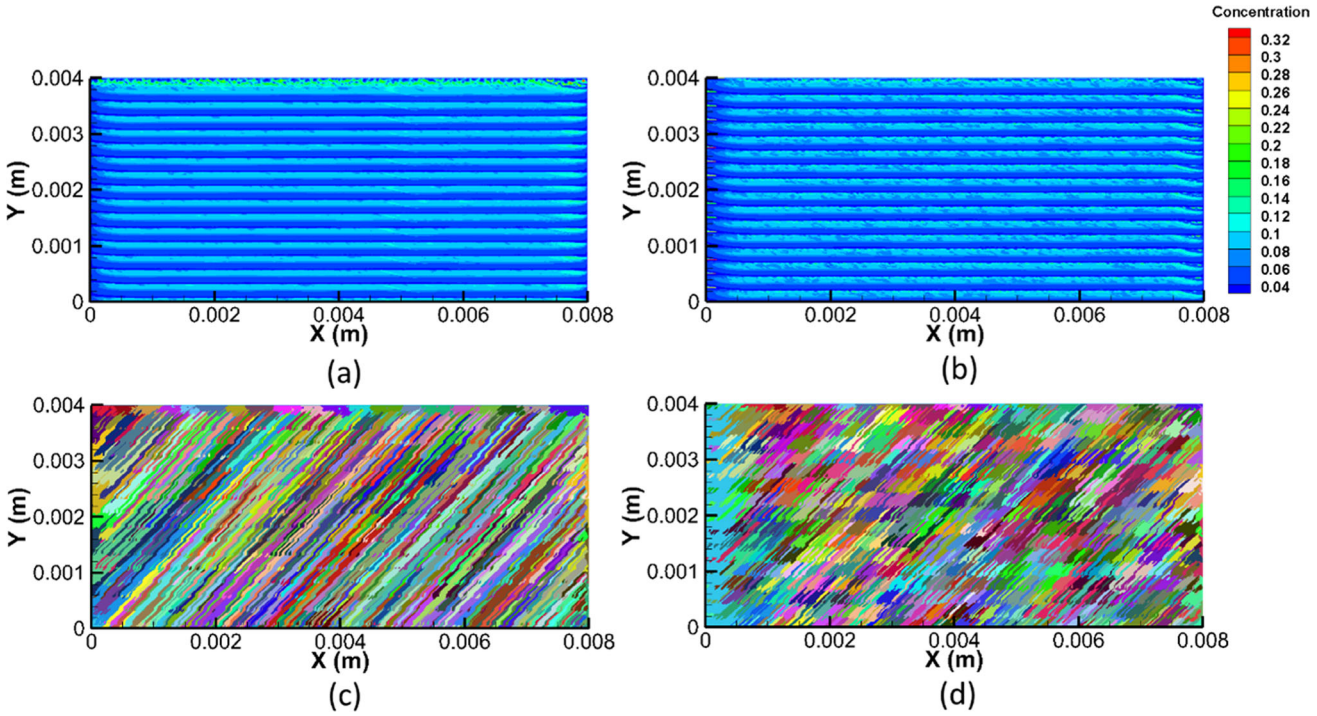

Fig. 9 Effect of laser spot radius: (a) solute concentration contours and (c) microstructure for r_0 = 0.05 mm (b) solute concentration contours and (d) microstructure for r_0 = 0.15 mm with P = 1000 W and v_l = 1.0 m/s for both

again for larger scan speeds, although the magnitude of variation is not very high. The grain density increases almost linearly with increasing laser scan speed. For a higher scan speed, the nucleation and growth of new grains in each layer leads to the increase of grain density.

One of the important parameters apart from laser power and scan speed is the laser spot radius at the surface of the sample. To study its effect, 5 cases are considered with a spot radius of 0.05, 0.08, 0.10, 0.12, and 0.15 mm. The laser power and travel speed are kept the same for all the cases. The values of all the other parameters are also same as stated in section 3.1. The concentration contours and grain structures for the lowest radius of 0.05 mm and highest radius of 0.15 mm are compared in Fig. 9. By comparing the top layers for both the cases, it can be surmised that the melt pool has a larger depth when the laser spot radius is less. Transfer of the same quantity of energy to a smaller zone leads to higher energy density and deeper melt pool. Also, because of this, it is seen that smaller radius results in elongated grains spanning multiple layers, while the opposite behavior is seen for the larger radius case.

Figure 10 shows the variation of SSD and grain density with the increase in spot radius. The grain density increases with the increase in spot radius due to the nucleation and growth of new grains in each layer. The SSD value decreases at first and then increases with increasing laser spot radius. The combined effect of change in grain density and change in the depth of melt pool may cause this variation in the species segregation.

4. Conclusions

In this paper, a numerical model for the simulation of melting and microstructure formation during a layer-by-layer laser melting process is presented. The model combines a sharp-interface enthalpy-based phase change model with domain transformation for tracking the melting and solidification in multiple layers. The species transport in the domain is also incorporated to track the segregation pattern for binary alloys.

Simulation results for Al-10% Cu show that the model can predict the change in grain structure and orientation due to changes in the laser scan direction, laser power, laser travel speed, and spot radius. It is seen that long elongated grains spanning multiple layers form when there is considerable remelting of the previous grains. Thus, higher power, lower travel speed and spot radius result in long grains with higher aspect ratio and lower grain density. The species segregation occurs in horizontal sections in each layer with lower

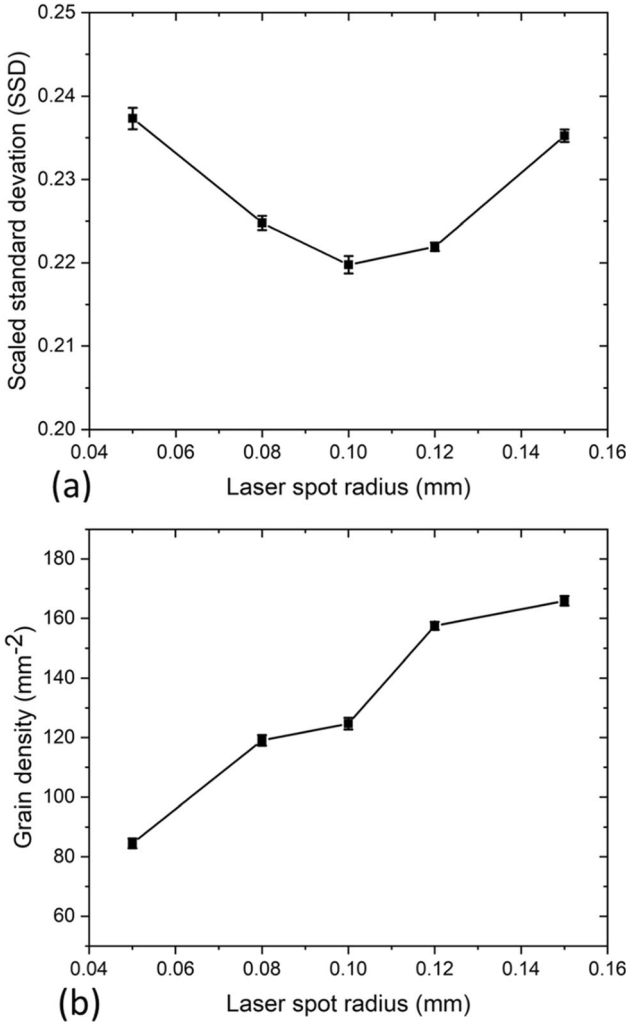

Fig. 10 Effect of laser spot radius on (a) SSD of species concentration and (b) grain density

concentration at the bottom of each layer and higher concentration at the upper section.

Funding

This work has been funded and supported by DST (Department of Science and Technology) SERB Project no. ECR/2017/002440.

Data Availability

The raw/processed data will be available on request.

Conflict of interest

None.

References

1. T. DebRoy, H.L. Wei, J.S. Zuback, T. Mukherjee, J.W. Elmer, J.O. Milewski, A.M. Beese, A.D. Wilson-Heid, A. De and W. Zhang, Additive Manufacturing of Metallic Components-Process, Structure and Properties, *Prog. Mater Sci.*, 2018, **92**, p 112–224.
2. D.D. Gu, W. Meiners, K. Wissenbach and R. Poprawe, Laser Additive Manufacturing of Metallic Components: Materials, Processes and Mechanisms, *Int. Mater. Rev.*, 2012, **57**(3), p 133–164.
3. D. Herzog, V. Seyda, E. Wycisk and C. Emmelmann, Additive Manufacturing of Metals, *Acta Mater.*, 2016, **117**, p 371–392.
4. E.O. Olakanmi, R.F. Cochrane and K.W. Dalgarno, A Review on Selective Laser Sintering/Melting (SLS/SLM) of Aluminium Alloy Powders: Processing, Microstructure, and Properties, *Prog. Mater Sci.*, 2015, **74**, p 401–477.
5. J.O. Milewski, *Additive Manufacturing of Metals*, Springer International Publishing, Cham, 2017
6. L.N. Carter, X. Wang, N. Read, R. Khan, M. Aristizabal, K. Essa and M.M. Attallah, Process Optimization of Selective Laser Melting Using Energy Density Model for Nickel Based Superalloys, *Mater. Sci. Technol.*, 2016, **32**(7), p 657–661.
7. C. Qiu, G.A. Ravi and M.M. Attallah, Microstructural Control During Direct Laser Deposition of a β-Titanium Alloy, *Mater. Des.*, 2015, **81**, p 21–30.
8. J. Zhao, B. Zhang, X. Li and R. Li, Effects of Metal-Vapor Jet Force on the Physical Behavior of Melting Wire Transfer in Electron Beam Additive Manufacturing, *J. Mater. Process. Technol.*, 2015, **220**, p 243–250.
9. P. Heinl, L. Müller, C. Körner, R.F. Singer and F.A. Müller, Cellular Ti-6Al-4V Structures with Interconnected Macro Porosity for Bone Implants Fabricated by Selective Electron Beam Melting, *Acta Biomater.*, 2008, **4**(5), p 1536–1544.
10. M.J. Bermingham, D. Kent, H. Zhan, D.H. StJohn and M.S. Dargusch, Controlling the Microstructure and Properties of Wire Arc Additive Manufactured Ti-6Al-4V with Trace Boron Additions, *Acta Mater.*, 2015, **91**, p 289–303.
11. F. Wang, S. Williams, P. Colegrove and A.A. Antonysamy, Microstructure and Mechanical Properties of Wire and Arc Additive Manufactured Ti-6Al-4V, *Metall. Mater. Trans. A.*, 2013, **44**(2), p 968–977.
12. M. Nahmany, I. Rosenthal, I. Benishti, N. Frage and A. Stern, Electron Beam Welding of AlSi10Mg Workpieces Produced by Selected Laser Melting Additive Manufacturing Technology, *Addit. Manuf.*, 2015, **8**, p 63–70.
13. C.A. Brice and W.H. Hofmeister, Determination Of bulk Residual Stresses in Electron Beam Additive-Manufactured Aluminum, *Metall. and Mater. Trans. A.*, 2013, **44**(11), p 5147–5153.
14. A. Yadollahi, N. Shamsaei, S.M. Thompson and D.W. Seely, Effects of Process Time Interval and Heat Treatment on the Mechanical and Microstructural Properties of Direct Laser Deposited 316L Stainless Steel, *Mater. Sci. Eng., A*, 2015, **644**, p 171–183.
15. M. Garibaldi, I. Ashcroft, M. Simonelli and R. Hague, Metallurgy of High-Silicon Steel Parts Produced Using Selective Laser Melting, *Acta Mater.*, 2016, **110**, p 207–216.
16. S.M. Kelly and S.L. Kampe, Microstructural Evolution in Laser-Deposited Multilayer Ti-6Al-4V Builds: Part I. Microstructural Characterization, *Metallur. Mater. Trans. A*, 2004, **35**(6), p 1861–1867.
17. T. Wang, Y.Y. Zhu, S.Q. Zhang, H.B. Tang and H.M. Wang, Grain Morphology evolution Behavior of Titanium Alloy Components During Laser Melting deposition Additive Manufacturing, *J. Alloy. Compd.*, 2015, **632**, p 505–513.
18. L.N. Carter, M.M. Attallah and R.C. Reed, Laser Powder Bed Fabrication of Nickel-Base Superalloys: Influence of Parameters; Characterization, Quantification and Mitigation of Cracking, *Superalloys*, 2012, **2012**(6), p 2826–2834.
19. L.E. Murr, E. Martinez, X.M. Pan, S.M. Gaytan, J.A. Castro, C.A. Terrazas, F. Medina, R.B. Wicker and D.H. Abbott, Microstructures of Rene 142 Nickel-Based Superalloy Fabricated by Electron Beam Melting, *Acta Mater.*, 2013, **61**(11), p 4289–4296.
20. W. Liu, K.M. Saleheen, Z. Tang, H. Wang, G. Al-Hammadi, A. Abdelrahman, Z. Yongxin, S.G. Hua and F. Wang, Review on Scanning Pattern Evaluation in Laser-Based Additive Manufacturing, *Opt. Eng.*, 2021, **60**(7), p 070901.
21. S. Das, Physical Aspects of Process Control in Selective Laser Sintering of Metals, *Adv. Eng. Mater.*, 2003, **5**(10), p 701–711.
22. W.E. King, A.T. Anderson, R.M. Ferencz, N.E. Hodge, C. Kamath, S.A. Khairallah and A.M. Rubenchik, Laser Powder Bed Fusion Additive Manufacturing of Metals; Physics, Computational, and Materials Challenges, *Appl. Phys. Rev.*, 2015, **2**(4), p 041304.
23. S.M. Thompson, L. Bian, N. Shamsaei and A. Yadollahi, An Overview of Direct Laser Deposition for Additive Manufacturing; Part I:

Transport Phenomena, Modeling and Diagnostics, *Addit. Manuf.*, 2015, **8**, p 36–62.
24. L.M. Sochalski-Kolbus, E.A. Payzant, P.A. Cornwell, T.R. Watkins, S.S. Babu, R.R. Dehoff, M. Lorenz, O. Ovchinnikova and C. Duty, Comparison of Residual Stresses in Inconel 718 Simple Parts Made by Electron Beam Melting and direct Laser Metal Sintering, *Metall. and Mater. Trans. A.*, 2015, **46**(3), p 1419–1432.
25. R. Rai, J.W. Elmer, T.A. Palmer and T. DebRoy, Heat Transfer and Fluid Flow During Keyhole Mode Laser Welding of Tantalum, Ti-6Al-4V, 304L Stainless steel and Vanadium, *J. Phys. D Appl. Phys.*, 2007, **40**(18), p 5753.
26. M.M. Collur, A. Paul and T. DebRoy, Mechanism of Alloying Element Vaporization During Laser Welding, *Metall. Trans. B*, 1987, **18**(4), p 733–740.
27. H. Qi, J. Mazumder and H. Ki, Numerical Simulation of Heat Transfer and Fluid Flow in Coaxial Laser Cladding Process for Direct Metal Deposition, *J. Appl. Phys.*, 2006, **100**(2), p 024903.
28. Y. Chew, J.H.L. Pang, G. Bi and B. Song, Thermo-Mechanical Model for Simulating Laser Cladding Induced Residual Stresses with Single and Multiple Clad Beads, *J. Mater. Process. Technol.*, 2015, **224**, p 89–101.
29. Z. Liu, D. Zhao, P. Wang, M. Yan, C. Yang, Z. Chen, J. Lu and Z. Lu, Additive Manufacturing of Metals: Microstructure Evolution and Multistage Control, *J. Mater. Sci. Technol.*, 2022, **100**, p 224–236.
30. C. Du, Y. Zhao, J. Jiang, Q. Wang, H. Wang, N. Li and J. Sun, Pore Defects in Laser Powder Bed Fusion: Formation Mechanism, Control Method, and Perspectives, *Journal of Alloys and Compounds*, 2023, **944**, p 169215.
31. W. Wang and S.Y. Liang, Prediction of Molten Pool Height, Contact Angle, and Balling Occurrence in Laser Powder Bed Fusion, *Int. J. Adv. Manuf. Technol.*, 2022, **119**(9–10), p 6193–6202.
32. G. Li, X. Li, C. Guo, Y. Zhou, Q. Tan, W. Qu, X. Li, X. Hu, M. Zhang and Q. Zhu, Investigation into the Effect of Energy Density on Densification, Surface Roughness and Loss of Alloying Elements of 7075 Aluminium Alloy Processed by Laser Powder Bed Fusion, *Opt. Laser Technol.*, 2022, **147**, p 107621.
33. J.J. Rindler, C.E. Slone, E.D. Herderick, M.J. Mills and A.J. Ramirez, Investigation on the Potential Effects of Laser Stitching and Subsequent Heat Treatment on the Microstructure and Mechanical Properties of Nickel Alloy 718 Produced via Laser Powder Bed Fusion (L-PBF), *Addit. Manuf.*, 2022, **57**, p 102906.
34. H. Xia, L. Li, C. Tan, J. Yang, H. Li, W. Song, K. Zhang, Q. Wang and N. Ma, In Situ SEM Study on Tensile Fractured Behavior of Al/Steel Laser Welding-Brazing Interface, *Mater. Des.*, 2022, **224**, p 111320.
35. B. Chen, Z. Wu, T. Yan, Z. He, B. Sun, G. Guo and S. Wu, Experimental Study on Mechanical Properties of Laser Powder Bed Fused Ti-6Al-4V Alloy Under Post-Heat Treatment, *Eng. Fract. Mech.*, 2022, **261**, p 108264.
36. S. Kou, Welding Metallurgy, *New Jersey USA*, 2003, **431**(446), p 223–225.
37. V. Ocelík, I. Furár and J.T.M. De Hosson, Microstructure and Properties of Laser Clad Coatings Studied by Orientation Imaging Microscopy, *Acta Mater.*, 2010, **58**(20), p 6763–6772.
38. S.A. David and J.M. Vitek, Correlation Between Solidification Parameters and Weld Microstructures, *Int. Mater. Rev.*, 1989, **34**(1), p 213–245.
39. M. Rappaz and C.A. Gandin, Probabilistic Modelling of Microstructure Formation in Solidification Processes, *Acta Metall. Mater.*, 1993, **41**(2), p 345–360.
40. W. Kurz, B. Giovanola and R. Trivedi, Theory of Microstructural Development During Rapid Solidification, *Acta Metall.*, 1986, **34**(5), p 823–830.
41. O. Hunziker, D. Dye and R.C. Reed, On the Formation of a Centreline Grain Boundary During Fusion Welding, *Acta Mater.*, 2000, **48**(17), p 4191–4201.
42. L. Thijs, K. Kempen, J.P. Kruth and J. Van Humbeeck, Fine-Structured Aluminium Products with Controllable Texture by Selective Laser Melting of Pre-Alloyed AlSi10Mg Powder, *Acta Mater.*, 2013, **61**(5), p 1809–1819.
43. B. Richter, N. Blanke, C. Werner, N.D. Parab, T. Sun, F. Vollertsen and F.E. Pfefferkorn, High-Speed X-ray Investigation of Melt Dynamics During Continuous-Wave Laser Remelting of Selective Laser Melted Co-Cr Alloy, *CIRP Ann.*, 2019, **68**(1), p 229–232.
44. J. Vaithilingam, R.D. Goodridge, R.J. Hague, S.D. Christie and S. Edmondson, The Effect of Laser Remelting on the Surface Chemistry of Ti6al4V Components Fabricated by Selective Laser Melting, *J. Mater. Process. Technol.*, 2016, **232**, p 1–8.
45. E.G. Brodie, A.E. Medvedev, J.E. Frith, M.S. Dargusch, H.L. Fraser and A. Molotnikov, Remelt Processing and Microstructure of Selective Laser Melted Ti25Ta, *J. Alloy. Compd.*, 2020, **820**, p 153082.
46. B. Liu, B.Q. Li and Z. Li, Selective Laser Remelting of an Additive Layer Manufacturing Process on AlSi10Mg, *Results in Physics*, 2019, **12**, p 982–988.
47. A. Boschetto, L. Bottini and D. Pilone, Effect of Laser Remelting on Surface Roughness and Microstructure of AlSi10Mg Selective Laser Melting Manufactured Parts, *Int. J. Adv. Manuf. Technol.*, 2021, **113**(9), p 2739–2759.
48. Z. Xiong, P. Zhang, C. Tan, D. Dong, W. Ma and K. Yu, Selective Laser Melting and Remelting of Pure Tungsten, *Adv. Eng. Mater.*, 2020, **22**(3), p 1901352.
49. M. Okugawa, Y. Ohigashi, Y. Furishiro, Y. Koizumi and T. Nakano, Equiaxed Grain Formation by Intrinsic Heterogeneous Nucleation via Rapid Heating and Cooling in Additive Manufacturing of Aluminum-Silicon Hypoeutectic Alloy, *J. Alloys Compd.*, 2022, **919**, p 165812.
50. M. Shiomi, A. Yoshidome, F. Abe and K. Osakada, Finite Element Analysis of Melting and Solidifying Processes in Laser Rapid Prototyping of Metallic Powders, *Int. J. Mach. Tools Manuf*, 1999, **39**(2), p 237–252.
51. N.K. Tolochko, M.K. Arshinov, A.V. Gusarov, V.I. Titov, T. Laoui and L. Froyen, Mechanisms of Selective laser Sintering and Heat Transfer in Ti Powder, *Rapid Prototyp. J.*, 2003, **9**(5), p 314–326.
52. K. Dai and L. Shaw, Thermal and Mechanical Finite Element Modeling of Laser forming from Metal and Ceramic Powders, *Acta Mater.*, 2004, **52**(1), p 69–80.
53. H. Yin and S.D. Felicelli, Dendrite Growth Simulation During Solidification in the LENS Process, *Acta Mater.*, 2010, **58**(4), p 1455–1465.
54. Z. Liu and H. Qi, Numerical Simulation of Transport Phenomena for a Double-Layer Laser Powder Deposition of Single-Crystal Superalloy, *Metall. and Mater. Trans. A.*, 2014, **45**(4), p 1903–1915.
55. A. Rai, M. Markl and C. Körner, A Coupled Cellular Automaton-Lattice Boltzmann Model for Grain Structure Simulation During Additive Manufacturing, *Comput. Mater. Sci.*, 2016, **124**, p 37–48.
56. A. Rai, H. Helmer and C. Körner, Simulation of Grain Structure Evolution During Powder Bed Based Additive Manufacturing, *Addit. Manuf.*, 2017, **13**, p 124–134.
57. A. Zinoviev, O. Zinovieva, V. Ploshikhin, V. Romanova and R. Balokhonov, Evolution of Grain Structure During Laser Additive Manufacturing. Simulation by a Cellular Automata Method, *Mater. Des.*, 2016, **106**, p 321–329.
58. J. Zhang, F. Liou, W. Seufzer and K. Taminger, A Coupled Finite Element Cellular Automaton Model to Predict Thermal History and Grain Morphology of Ti-6Al-4V During Direct Metal Deposition (DMD), *Addit. Manuf.*, 2016, **11**, p 32–39.
59. T.M. Rodgers, J.D. Madison and V. Tikare, Simulation of Metal Additive Manufacturing Microstructures Using Kinetic Monte Carlo, *Comput. Mater. Sci.*, 2017, **135**, p 78–89.
60. J.G. Pauza, W.A. Tayon and A.D. Rollett, Computer Simulation of Microstructure Development in Powder-Bed Additive Manufacturing with Crystallographic Texture, *Modell. Simul. Mater. Sci. Eng.*, 2021, **29**(5), p 055019.
61. S. Sahoo and K. Chou, Phase-Field Simulation of Microstructure Evolution of Ti-6Al-4V in Electron Beam Additive Manufacturing Process, *Addit. Manuf.*, 2016, **9**, p 14–24.
62. Sethian, J. A. (1996). Level Set Methods: Evolving Interfaces in Geometry, Fluid Mechanics. *Computer Vision, and Materials Science*
63. V.R. Voller, An Enthalpy Method for Modeling Dendritic Growth in a Binary Alloy, *Int. J. Heat Mass Transf.*, 2008, **51**(3–4), p 823–834.
64. M. Jegatheesan and A. Bhattacharya, An Enthalpy Based Model for Microstructure Evolution During Binary Alloy Solidification, *Comput. Mater. Sci.*, 2021, **186**, p 110072.
65. A. Bhattacharya and P. Dutta, An Enthalpy-Based Model of Dendritic Growth in a Convecting Binary Alloy Melt, *Int. J. Numer. Methods Heat Fluid Flow.*, 2013, **23**, p 1121–1135.
66. A. Swain, P.M. Khan, P. Rath and A. Bhattacharya, Modeling Layer-by-Layer Laser Melting and Solidification of Binary Alloy Powder Bed, *J. Laser Appl.*, 2021, **33**(4), p 042040.

67. S.V. Patankar, *Numerical Heat Transfer and Fluid Flow*, CRC Press, 2018
68. L.L. Parimi, G.A. Ravi, D. Clark and M.M. Attallah, Microstructural and Texture Development in Direct Laser Fabricated IN718, *Mater. Charact.*, 2014, **89**, p 102–111.
69. F. Xu, F. Xiong, M.J. Li and Y. Lian, Three-Dimensional Numerical Simulation of Grain Growth during Selective Laser Melting of 316L Stainless Steel, *Materials*, 2022, **15**(19), p 6800.
70. H.L. Wei, J. Mazumder and T. DebRoy, Evolution of Solidification Texture During Additive Manufacturing, *Sci. Rep.*, 2015, **5**(1), p 1–7.
71. H.L. Wei, J.W. Elmer and T. DebRoy, Three-Dimensional Modeling of Grain Structure Evolution During Welding of an Aluminum Alloy, *Acta Mater.*, 2017, **126**, p 413–425.
72. A.R.A. Dezfoli, W.S. Hwang, W.C. Huang and T.W. Tsai, Determination and Controlling of Grain Structure of Metals After Laser Incidence: Theoretical Approach, *Sci. Rep.*, 2017, **7**(1), p 41527.
73. E. Jelis, M.R. Hespos, M. Feurer and S. Groeschler, Development of Laser Powder Bed Fusion Processing Parameters for Aermet 100 Powder, *J. Mater. Eng. Perform.*, 2022 https://doi.org/10.1007/s11665-022-07638-y
74. L.E. Criales, Y.M. Arısoy, B. Lane, S. Moylan, A. Donmez and T. Özel, Laser Powder Bed Fusion of Nickel Alloy 625: Experimental Investigations of Effects of Process Parameters on Melt Pool Size and Shape with Spatter Analysis, *Int. J. Mach. Tools Manuf*, 2017, **121**, p 22–36.
75. S.K. Nayak, S.K. Mishra, A.N. Jinoop, C.P. Paul and K.S. Bindra, Experimental Studies on Laser Additive Manufacturing of Inconel-625 Structures Using Powder Bed Fusion at 100 μm Layer Thickness, *J. Mater. Eng. Perform.*, 2020, **29**, p 7636–7647.
76. T.M. Wischeropp, H. Tarhini and C. Emmelmann, Influence of Laser Beam Profile on the Selective Laser Melting Process of AlSi10Mg, *J. Laser Appl.*, 2020, **32**(2), p 022059.
77. Z. Sun, X. Tan, S.B. Tor and W.Y. Yeong, Selective Laser Melting of Stainless Steel 316L with Low Porosity and High Build Rates, *Mater. Des.*, 2016, **104**, p 197–204.
78. M.C. Sow, T. De Terris, O. Castelnau, Z. Hamouche, F. Coste, R. Fabbro and P. Peyre, Influence of Beam Diameter on Laser Powder Bed Fusion (L-PBF) Process, *Addit. Manuf.*, 2020, **36**, p 101532.